coatings

MDPI

Article

In Situ Deposition of Reduced Graphene Oxide on Ti Foil by a Facile, Microwave-Assisted Hydrothermal Method

Carmen Lazau [1], Mircea Nicolaescu [1,2], Corina Orha [1], Aniela Pop [2], Simona Căprărescu [3] and Cornelia Bandas [1,*]

[1] National Institute for Research and Development in Electrochemistry and Condensed Matter Timisoara, Dr. A.P. Podeanu No. 144, 300569 Timisoara, Romania
[2] Department of Applied Chemistry and Engineering of Inorganic Compounds and Environment, University "Politehnica" of Timisoara, P-ta Victoriei No. 2, 300006 Timisoara, Romania
[3] Department of Inorganic Chemistry, Physical Chemistry and Electrochemistry, Faculty of Chemical Engineering and Biotechnologies, University "Politehnica" of Bucharest, Polizu Street No. 1–7, 011061 Bucharest, Romania
* Correspondence: cornelia.bandas@gmail.com

Abstract: Reduced graphene oxide (rGO) was successfully deposited in situ onto Ti foil via a microwave-assisted hydrothermal method for the development of Ti-TiO_2-rGO composite structures. The TiO_2 crystallin layer was produced by the thermal oxidation of titanium foil in the presence of 0.5 M hydrofluoric acid in a controlled atmosphere consisting of a mixed flow gas of Ar and O_2 at 500 °C. A great advantage of using the microwave-assisted hydrothermal method for obtaining composite structures is the fast and uniform heating mode, which prevents the aggregation of graphene layers. Specific analyses, such as X-ray diffraction, UV-VIS analysis, and SEM morphology, were used to investigate the structural, optical, and morphological characteristics of the composites. The *I-V* measurements of the Ti-TiO_2-rGO composite structures were performed using forward bias with an applied voltage between −3 V and +3 V and a step rate of 10 mV/s. Moreover, the electrochemical behavior was obtained by cyclic voltammetry in a 1 M KNO_3 supporting electrolyte and in the presence of 4 mM $K_3Fe(CN)_6$ to determine the electroactive surface area and apparent diffusion coefficient. The charge transfer resistance was investigated via electrochemical impedance spectroscopy (EIS) in a 0.1 M Na_2SO_4 supporting electrolyte and within a frequency range of 100 kHz to 0.1 Hz to confirm the role of rGO on the electrode's surface. This study provided new insights into the development of high-performance and cost-effective Ti-TiO_2-rGO structures both for the development of electrochemical electrodes and gas sensors.

Keywords: reduced graphene-oxide; TiO_2; microwave reaction; in situ deposition

check for updates

Citation: Lazau, C.; Nicolaescu, M.; Orha, C.; Pop, A.; Căprărescu, S.; Bandas, C. In Situ Deposition of Reduced Graphene Oxide on Ti Foil by a Facile, Microwave-Assisted Hydrothermal Method. *Coatings* **2022**, *12*, 1805. https://doi.org/10.3390/coatings12121805

Academic Editor: Enikö György

Received: 31 October 2022
Accepted: 22 November 2022
Published: 23 November 2022

1. Introduction

Graphene is one of the most promising advanced carbon-based nanomaterials due to its extraordinary electronic transport properties, large surface area, and high electrocatalytic activity. Graphene has been widely used in various fields such as photocatalysts, lithium battery electrodes, supercapacitors, sensors, and electronic devices [1,2]. Most of the graphene used in electrochemistry is produced from the reduction of graphene oxide and usually has functional groups, such as hydroxyl and carboxyl, which are advantageous for adsorbing heavy metal ions. Reduced graphene oxide (rGO), which plays the role of a p-type semiconductor, can form heterojunctions when forming composites with most metal-oxide semiconductors [3].

GO nanosheets decorated with metal oxide nanoparticles combine the outstanding features of each because of the synergistic effect between them. Metal oxide semiconductors, such as tin oxide (SnO_2) [4], titanium dioxide (TiO_2) [5], zinc oxide (ZnO) [6], copper oxide (CuO) [7], tungsten oxide (WO_3) [8,9], indium oxide (In_2O_3) [10], molybdenum sulfide (MoS_2) [11], ferric oxide (Fe_2O_3) [12], and cobalt oxide (Co_3O_4) [13] possess many

outstanding advantages such as high sensitivity, fast response/recovery times, and low cost, such that they are often used as important materials for gas sensors. The synergistic effects of graphene hybridization with metal oxides revealed high levels of electrochemical properties, helping to improve the selectivity and sensitivity of the electrochemical sensor. The formation of p-n heterojunction nanocomposites could modify and engineer the gas-sensing capabilities of gas sensors by changing the electrical performance near the heterointerfaces. In addition, the large specific surface area of the nanocomposites could provide more available active sites and promote gas adsorption for specific oxygen adsorption to design a gas sensor with high responsiveness.

Recently, several efficient synthesis methods for GO-based metal oxides have been studied to obtain materials with a controlled shape and stability, and that are monodispersed via chemical precipitation, selfassembly, sol-gel, microwave irradiation, solution mixing method, direct growth of metal oxide nanoparticles on the surface of graphene oxide, and hydrothermal synthesis techniques [14,15]. Yoon et al. synthesized GO and rGO composites via the chemical precipitation of the Fe_3O_4 precursor in GO and rGO solutions to study the comparative evaluation of magnetite-graphene oxide and magnetite-reduced graphene oxide for the removal of As(III) and As(V), establishing a high adsorption capacity (of M-GO and M-rGO toward As(III) and As(V)) [16]. Chandra et al. studied the removal of arsenic from weather conditions using magnetite rGO hybrids, synthesized by a chemical reaction with the nanosized Fe_3O_4 particle (10 nm). These compounds show almost complete (over 99.9%) arsenic removal up to 1 ppb due to the high binding capacity of As(III) and As(V) in the as-synthesized compound [17]. Another study shows the highly selective adsorption of lead ions from water by magnetic chitosan/graphene oxide materials fabricated through a facile and fast process of chemical precipitation. Their research showed that the synthesis materials are a viable alternative in the removal of Pb^{2+} from agricultural and industrial wastewater because of the increased surface area of the composite material, enhancing the stability, adsorption capacity (76.94 mg/g), and desorption capacity (90.3%) [18]. Liu et al. synthesized (via selfassembly) a porous Fe_3O_4 hollow microsphere/graphene oxide composite for the removal of Cr(VI), with a higher sorption capacity for the Cr(VI) ions from water [19]. Liu et al. presented a novel approach for the removal of heavy metal ions using a three-dimensional (3D) graphene/δ-MnO_2 aerogel, fabricated via selfassembly and the reduction of graphene oxide followed by the in situ solution-phase deposition of ultrathin δ-MnO_2 nanosheets [20]. Babu et al. focused on the characterization of a composite of rGO and mesoporous Fe_2O_3/TiO_2 nanoparticles via a sol-gel process for the removal of As(III) and As(V) from potable water. A clear influence of the pH of the solution on the adsorption capacity was revealed, proving that an rGO-MFT solution with a pH of 6 is the best for As(III) and As(V) [21]. A simple hydrothermal method for the synthesis of a nanocomposite rGO/ZrO_2 used to remove fluoride from aqueous solutions was prepared by Mohan et al. The results showed a large surface area, which makes a remarkable adsorption capacity for the composite synthesized via a hydrothermal process [22].

Another paper reported the electrochemical deposition of ZnO nanorods and *p*-type and *n*-type Cu_2O films on rGO films, which were coated on flexible polyethylene terephthalate (PET) substrates. The authors believed that the functional material deposited on a flexible rGO-PET film makes it suitable for electronic device applications, such as solar cells [23]. Similarly, Tai et al. deposited ZnO nanoparticles and GO thin films on gold interdigital electrodes (IDEs) through a simple spray process and thermally reduced the deposits of the ZnO–rGO composites. The composite sensor with the optimal amount of GO was highly sensitive to low concentrations of NH_3 and responded dramatically, which could be attributed to the p–n heterojunctions formed between ZnO and rGO [24]. Fauzi et al. demonstrated a mixed-potential-type gas sensor using a Ce-intercalated GO membrane fitted with an Au-WO_3/rGO electrode for the detection of ethanol at a low ppb level in air at room temperature; the main drawback of this sensor was its slow response and recovery [25]. Zhang et al. synthesized CuO nanoflowers via the hydrothermal

method, and then CuO and rGO were deposited on the substrate with Ni/Cu IDEs to fabricate the CuO-rGO sensor. The CuO–rGO sensor showed a higher sensitivity to CO and a faster response/recovery time than the rGO sensor, while the pure CuO sensor showed no response to CO at room temperature [26]. Over time, some researchers have studied the electrochemical properties of rGO-TiO_2 nanocomposites for application in photoelectrochemical detection processes [27,28]. Arfin et al. presented a ZnO functionalized GO modified glassy carbon electrode (GO–ZnO/GCE), which was used for the electrochemical sensory detection of phenol. The results revealed that GO–ZnO exhibited favorable electrochemical behavior for phenol oxidation, which was assigned to the joint efficiency of the properties of ZnO and GO [29]. Another study demonstrated that the aptasensor rGO-TiO_2 acts as an excellent biosensing platform that offers a reliable, rapid, and sensitive alternative for foodborne pathogen detection [30]. Vajedi and Dehghani have studied TiO_2/rGO nanocomposites that were modified GCEs for the electrochemical detection of Cd (II), Pb (II), and Cu (II), and concluded that the improved electrochemical performance of the electrode based on TiO_2/rGO could be attributed to the presence of GO that enhances electrochemical properties [31]. In this study, a Ti-TiO_2-rGO composite structure was obtained in situ by a simple and low-cost synthesis process: a microwave-assisted hydrothermal method. To the best of our knowledge, there are no reported works on the in situ synthesis of Ti-TiO_2-rGO structures in microwave-assisted hydrothermal conditions via the deposition of graphene oxide (GO) on a titanium foil support. This work provided new perspectives on obtaining high-performance and cost-effective Ti-TiO_2-rGO composite structures obtained in microwave-assisted hydrothermal conditions that could be used in both the development of electrochemical electrodes for the detection of pollutants and as gas sensors.

2. Materials and Methods

2.1. Reagents

Synthesis reagents were as follows: graphene oxide 4 mg/mL dispersed in H_2O, titanium foil (99.99% purity), titanium isopropoxide (TTIP, 98%), hydrofluoric acid (HF) solution (0.5 M), acetone, ethyl alcohol; all were used without any previous treatment, purchased from Sigma-Aldrich Company (St. Louis, MO, USA).

2.2. Synthesis of Ti-TiO_2-rGO Composite Structures

The Ti-TiO_2-rGO composite structures were achieved as illustrated in Figure 1. Firstly, the crystalline TiO_2 layers were grown on the titanium (Ti) foil by thermal oxidation, as previously reported in our research paper [32], carried out in a controlled atmosphere consisting of a mixed gas flow of 95% Ar and 5% O_2. Depending on the etching times, the supports were named: Ti-TiO_2-1h, Ti-TiO_2-2h, and Ti-TiO_2-3h. Secondly, the Ti-TiO_2-rGO composites structures were obtained in situ by microwave-assisted hydrothermal method as described: An aqueous solution containing 0.5 mL TTIP, 2 mL ethanol, and 3 mL GO was stirred for 30 min and ultrasounded for 15 min to form a homogenous mixture at room temperature; afterward, the mixture, together with Ti-TiO_2 supports (1×1.5 cm^2), was transferred into a 100 mL quartz autoclave with 10% fullness degree in a microwave-assisted hydrothermal reaction (Multiwave 3000 Microwave Digestion Oven, Anton Paar, Graz, Austria). The microwave-assisted hydrothermal treatment was applied by using a temperature of 200 °C for 60 min (with an increase in gradient temperature of 20 min), and the power of the microwave oven was about 1200 W. Finally, when the quartz autoclave was cooled in air, the as-obtained composite structures were washed with distilled water and dried at 50 °C for 30 min. The as-synthesized composite structures were coded as follows: Ti-TiO_2-rGO-1h, Ti-TiO_2-rGO-2h, and Ti-TiO_2-rGO-3h.

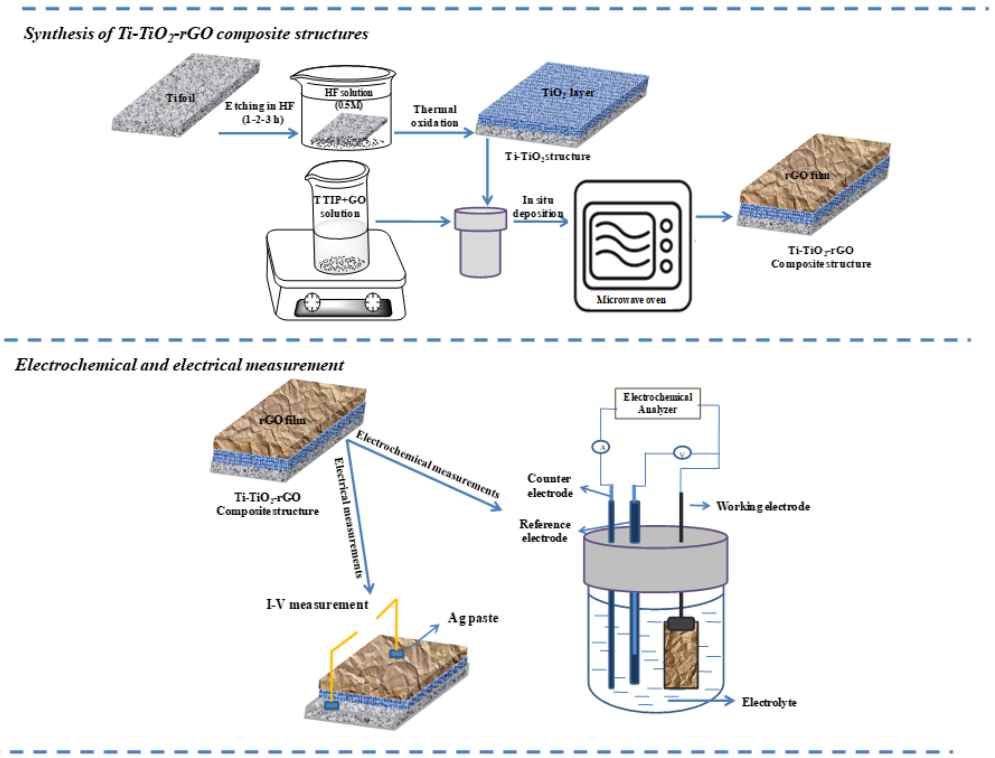

Figure 1. Schematic illustration of the achievement process for composite structures.

2.3. Materials Characterization

X-ray diffraction analysis (XRD, PANalytical X'Pert PRO MPD Diffractometer, PANalytical Company, Almelo, Netherlands) with Cu-Kα radiation in the range *2theta* = 20–80° was used for the crystalline structure of the composite structures. The morphology of the composite structures was examined using scanning electron microscopy (SEM, FEI Inspect S model, FEI Company, Eindhoven, Netherlands). The optical properties were recorded using UV-VIS analysis (PerkinElmer Lambda 950 UV/Vis spectrophotometer, Shelton, CT, USA) with an integrating sphere in the range of 300–600 nm. Electrical measurements for the obtained composite structures were performed using the Keithley 2450 SourceMeter SMU Instrument (Keithley, Oldbury, UK) in forward bias with an applied voltage between −3 V and +3 V, and a step rate of 10 mV/s. To collect data, the metal wires were affixed with silver paste and the location of the electrical contacts is presented in Figure 1. For electrochemical measurements, an Autolab potentiostat/galvanostat (PGSTAT 302 Autolab B.V., Metrohm, Utrecht, Netherlands) controlled with GPES 4.9 software using a three-electrode cell system in 1M KNO_3 solution was used. The samples prepared on Ti foil (an effective area of 1.5 cm^2) acted as the working electrodes; Ag/AgCl served as the reference electrode, and platinum acted as the counter electrode.

3. Results and Discussion

3.1. Structural and Morphological Characteristics

The X-ray patterns for the Ti-TiO_2 layers, the Ti-TiO_2-rGO composite structures, and the pure rGO are presented in Figure 2. It can be seen that, in Figure 2a, there are strong peaks at *2theta* values of 27.4°, 36.1°, 54.41°, and 63.06°, corresponding to rutile-TiO_2 (JCPDS No. 01-073-1765), crystallized after the thermal oxidation of Ti foil. Moreover, the specific peaks of the Ti element were identified at a *2theta* of 35.1°, 38.4°, 40.2°, 53.04°, 63.06°, 70.7°, and 76.4° (JCPDS No. 00-044-1294). The weak diffraction peak of the Ti-TiO_2-rGO composite structures at a *2theta* of 25.3° corresponds to the (101) of anatase-TiO_2 (JCPDS No. 01-083-2243), formed during the synthesis in the microwave-assisted hydrothermal reaction (Figure 2b). The peaks of rGO are difficult to identify because of the high intensity

of the diffraction peaks from the Ti foil. Figure 2c shows the X-ray pattern of the pure rGO, and a *2theta* value of 23.7° confirms the existence of rGO [33,34]. Furthermore, the broad and dispersive diffraction peak at around 23.7° of the Ti-TiO_2-rGO composite structures confirms the presence of rGO [35].

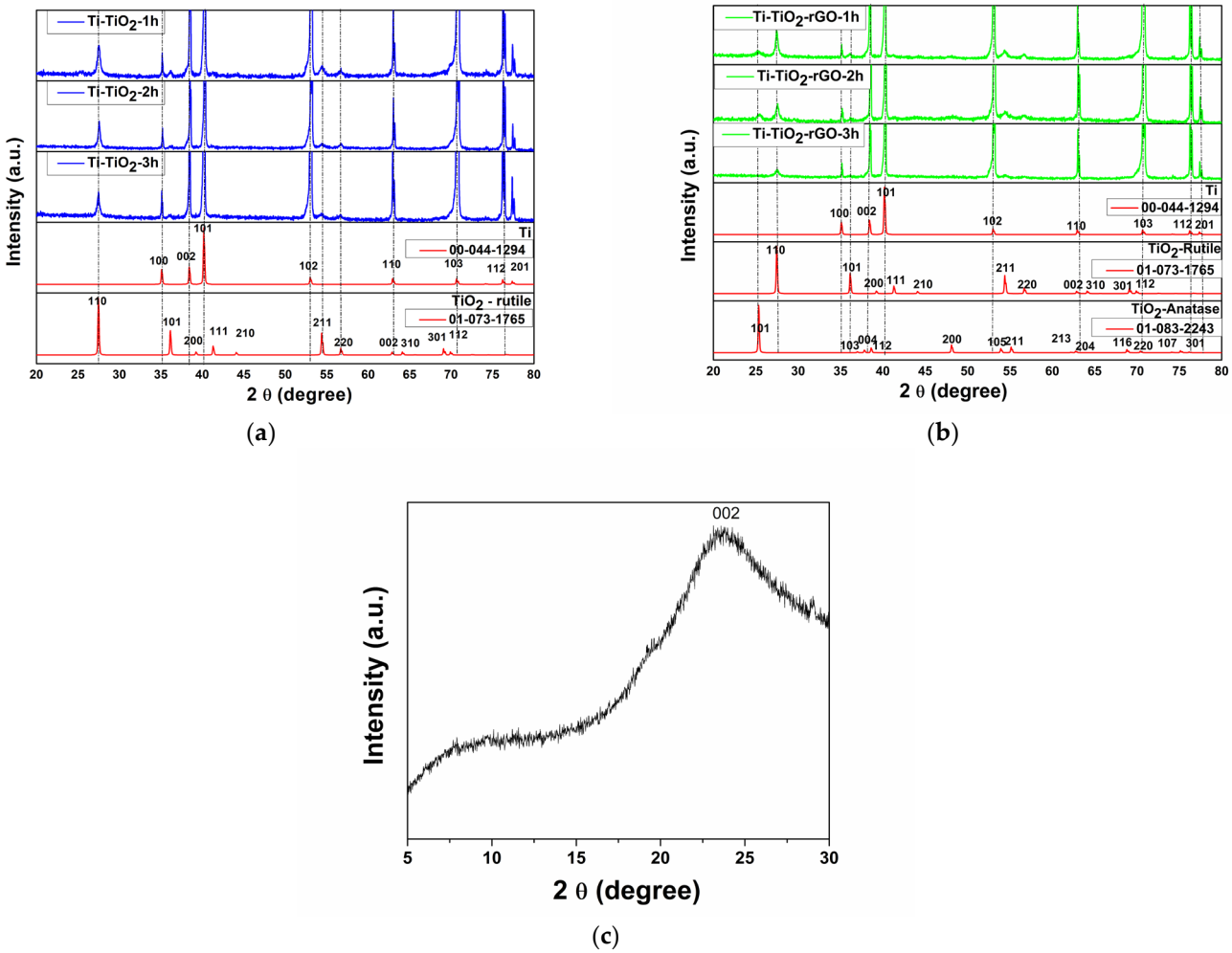

Figure 2. X-ray patterns of the as-obtained structures; (**a**) Ti-TiO_2 layers; (**b**) Ti-TiO_2-rGO composites; (**c**) pure rGO.

Figure 3 shows the surface morphologies of the Ti-TiO_2 layers and the Ti-TiO_2-rGO composite structures. The results revealed that, for the Ti-TiO_2 layers, the HF concentration and the etching time caused the complete removal of the passivation layer from the surface of the Ti foil for all Ti-TiO_2 samples (Figure 3a,c,e). Therefore, the Ti-TiO_2 layers have the appearance of broken stone, and the growth was clearly oriented in a defined direction. In addition, it can be seen that the rGO sheets cover the Ti-TiO_2 layer, and the rGO films have the appearance of slightly wrinkled flakes that appear to be stacked together, which is more pronounced for the Ti-TiO_2-rGO-2h (Figure 3d) and Ti-TiO_2-rGO-3h (Figure 3f) composite structures. This aspect is probably due to the morphology of the Ti-TiO_2 layers, where the appearance of broken stones is more pronounced due to the longer etching time.

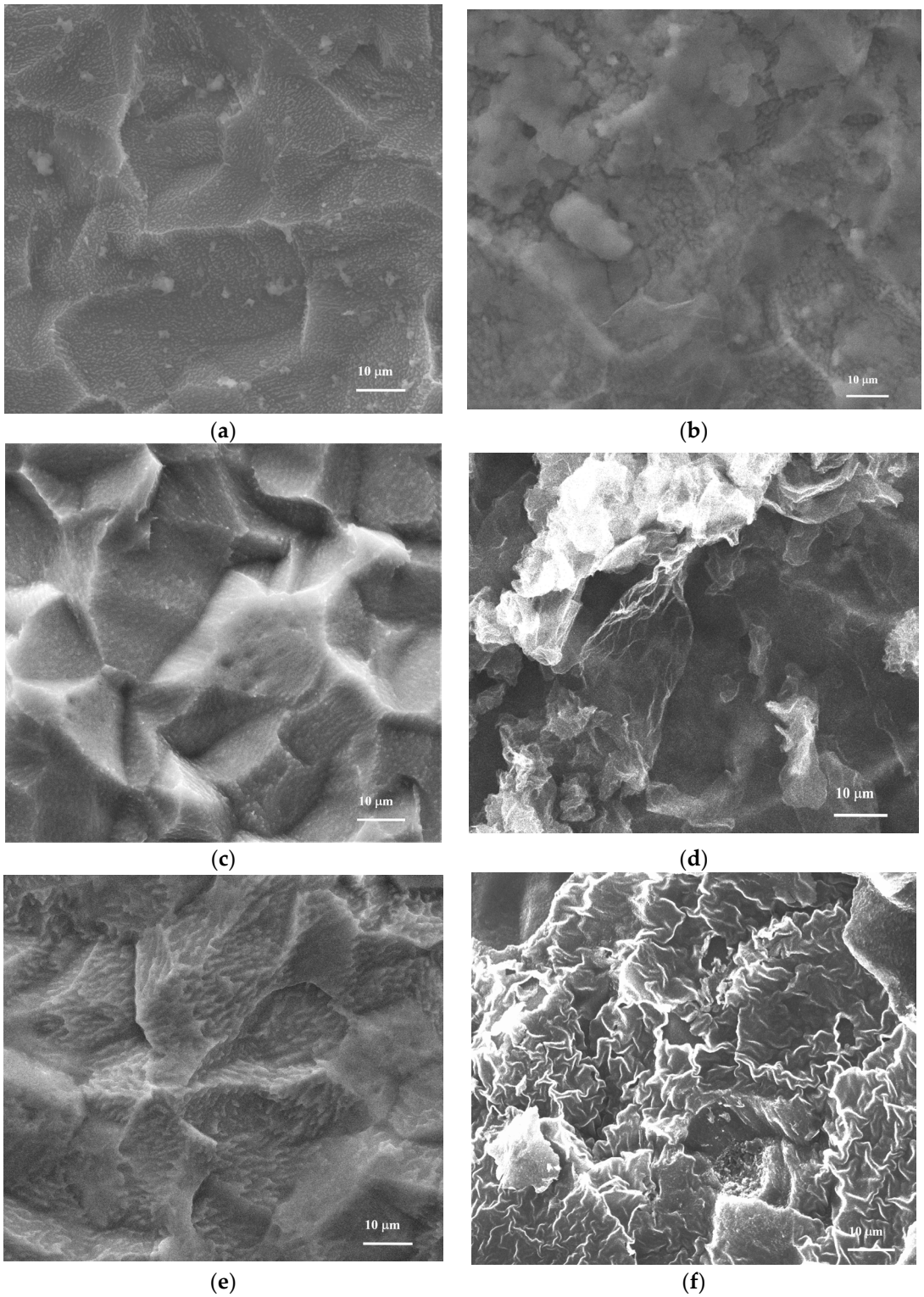

Figure 3. SEM images of (**a**) Ti-TiO_2-1h, (**b**) Ti-TiO_2-rGO-1h, **(c)** Ti-TiO_2-2h, (**d**) Ti-TiO_2-rGO-2h, (**e**) Ti-TiO_2-3h, and (**f**) Ti-TiO_2-rGO-3h.

3.2. Optical and Electrical Properties

The optical absorption spectra of the Ti-TiO_2-rGO composites in the range of 300–600 nm are shown in Figure 4. The optical band gap energy of the materials was determined using the Kubelka–Munk absorbance calculated by the *Tauc* plot, as shown in Figure 4b. The *Eg* optical bandgap energy was derived from the intersection of the straight line with the

hv-axis of the *Tauc* plot. Compared to the bandgap value of the Ti-TiO_2 layers (*Eg* = 2.95 eV) that were previously reported in our research [32] and that correspond to the rutile-TiO2 form, the bandgap slightly decreased due to the presence of rGO for Ti-TiO_2-rGO-1h, up to the value *Eg* = 2.68 eV, for Ti-TiO_2-rGO-2h, up to the value *Eg* = 2.87 eV, and for Ti-TiO_2-rGO-3h, up to the value *Eg* = 3.15 eV (Figure 4b). According to the literature data, the shifting in the valence band is attributed to the Ti-O-C bonds, and furthermore, the modification of the spectra shown in Figure 4a confirms the interface between TiO_2 and rGO, respectively [36].

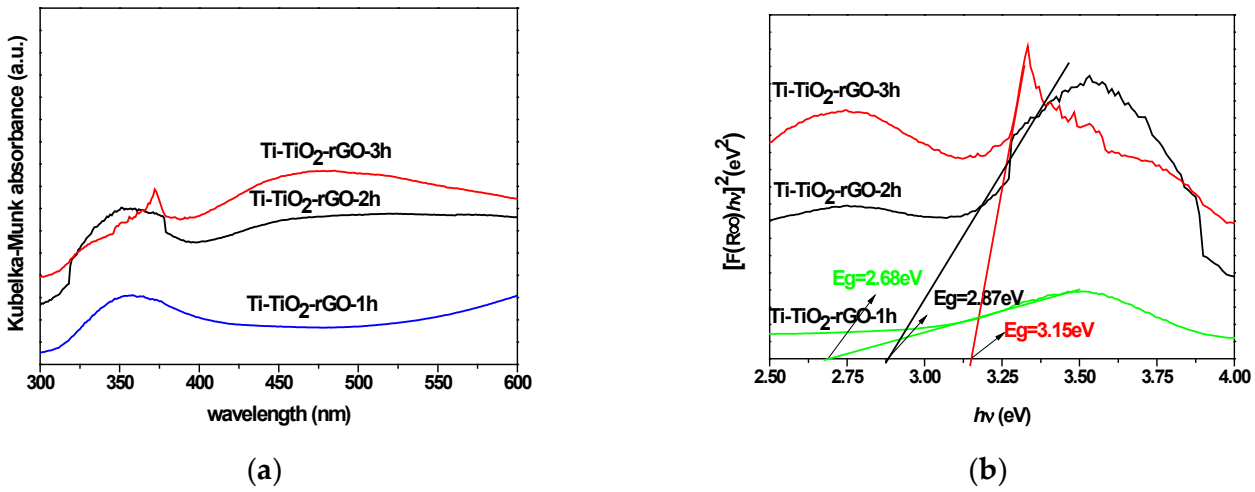

(**a**) (**b**)

Figure 4. Kubelka–Munk absorbance for the Ti-TiO_2-rGO composites (**a**); plot of $[F(R)*h\nu]^2$ versus the energy for composites structures (**b**).

The current-voltage characteristics of the *n*-TiO_2/*p*-rGO heterojunction were investigated at room temperature and are shown in Figure 5. Figure 5a,c,e present the influence of the etching time of Ti foil on the *I-V* curve of the as-obtained TiO_2/rGO heterojunction. As presented in our previous paper, an obvious influence of the fabrication parameters can be observed [32]. A rectifying behavior between the forward and reverse biases is achieved for all the synthesized samples, with a high rectification ratio (RR) ($I_{Forward}/I_{Reverse}$) of 35.76 at ± 3 V observed for the Ti-TiO_2-rGO-1h composite, which is much higher than that of Ti-TiO_2- rGO-2h (1.14 at ± 3 V). In the case of the Ti-TiO_2-rGO-3h composite structure, the RR is less than 1 (0.54 at ± 3 V), which is due to the increase in the reverse bias current. From the *I-V* curve, a slight increase in the turn-on voltage of Ti-TiO_2-rGO-1h at 1.668 V to 1.908 V for the Ti-TiO_2-rGO-2h structure is observed. The turn-on voltage of the Ti-TiO_2-rGO-3h composite is greater than the testing domain ± 3 V.

Figure 5b,d,f present a *Log (I)–V* between the forward and reverse biases of the composite structures. The rectifying nature of the TiO_2/rGO heterojunction and an increase in the asymmetry between the forward and reverse biases is highlighted more for the Ti-TiO_2-rGO-1h structure, as presented in Figure 5b; for the Ti-TiO_2-rGO-2h and Ti-TiO_2-rGO-3h structures, a slight rectification behavior appeared (Figure 5d,f) [37]. In order to evaluate the characteristics of the TiO_2/rGO junction, the thermionic emission relation from the current-voltage was used [38]. From the *Log (I)-V* plot (Figure 5b,d,f), the ideality factor (n) and the reverse saturation current (I_0) are calculated as per our previous research [32]. The heterojunction working parameters are presented in Table 1.

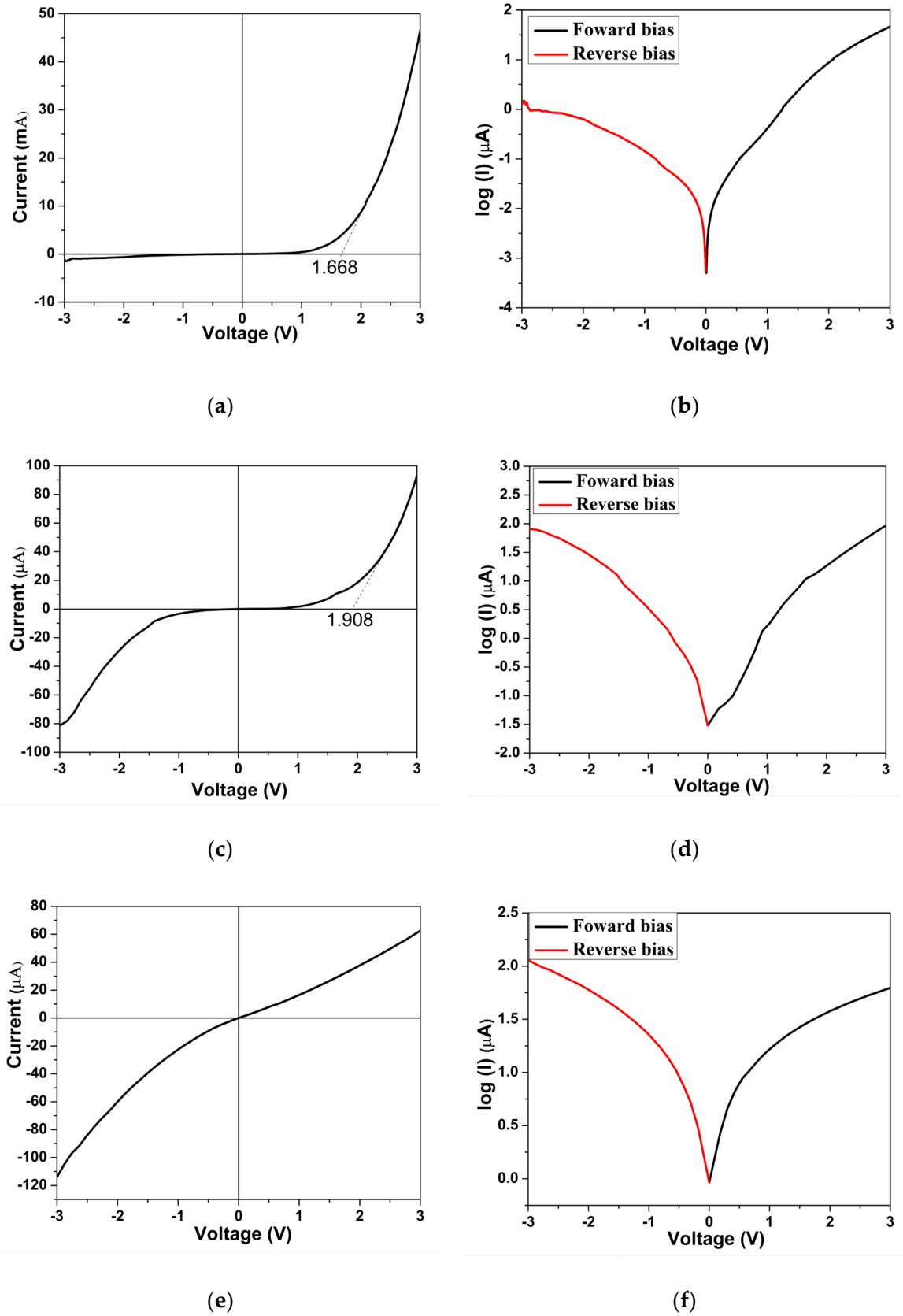

Figure 5. Current-voltage characteristics of the *n*-TiO_2/*p*-rGO heterojunction for (**a**) Ti-TiO_2-rGO-1h, (**c**) Ti-TiO_2-rGO-2h, and (**e**) Ti-TiO_2-rGO-3h; *Log* from forward and reverse bias for (**b**) Ti-TiO_2-rGO-1h, (**d**) Ti-TiO_2-rGO-2h, and (**f**) Ti-TiO_2-rGO-3h.

Table 1. Electrical parameters of the *n*-TiO_2/*p*-rGO heterojunction.

Composite Structure	V_T (V)	I_F (μA)	I_R (μA)	n	I_0 (A)
Ti-TiO_2-rGO-1h	1.668	46.5	−1.3	2.31	24.28×10^{-9}
Ti-TiO_2-rGO-2h	1.908	92.9	−81.3	15.51	8.93×10^{-9}
Ti-TiO_2-rGO-3h	-	43.3	−79.5	16.81	1.02×10^{-9}

It is generally presented in the literature data that ideality factors that are greater than 2 can be attributed to a complex recombination process in the quasineutral zone [39]. The results for the TiO_2/rGO heterojunction show that the surface modification of the etching process directly influences the ideality factor [40]. In this study, the higher values of *n* (15.51 and 16.81) for the Ti-TiO_2-rGO-2h and Ti-TiO_2-rGO-3h structures indicate that they may undergo several more recombination processes, dramatically incising the ideality factor. For Ti-TiO_2-rGO-1h, an ideality factor of about 2.31, which is very close to the normal range ($1 < n < 2$), is clearly highlighted with a reduced number of traps/defects in the quasineutral zone [38,41]. The move of the junction away from an ideal value can be explained by the growth of the surface area and the TiO_2 layer generated by the increase in the etching time. The significant decrease in the reverse saturation current by many orders of magnitude may explain the increase in traps/defects in the Ti-TiO_2-rGO-2h and Ti-TiO_2-rGO-3h structures.

3.3. Electrochemical Performance of the Ti-TiO_2-rGO Structure

The electrochemical behavior of the Ti-TiO_2-rGO composite structures as electrode materials was assessed using the cyclic voltammetry technique in the presence of the ferro/ferricyanide redox couple as an electrochemical model of a reversible redox system, used to determine the electroactive surface area of the working electrode and the apparent diffusion coefficient. Figure 6 shows the cyclic voltammograms recorded for the tested Ti-TiO_2-rGO composite structures at different scanning rates (i.e., 0.025, 0.05, 0.1, 0.2, and 0.3 Vs^{-1}) in a 1M KNO_3 supporting electrolyte and in the presence of 4 mM $K_3Fe(CN)_6$. Moreover, in the Supplementary Materials (Figure S1a–f), we present the cyclic voltammograms recorded in a 1M KNO_3 supporting electrolyte and in the presence of 4 mM $K_3Fe(CN)_6$ for the Ti-TiO_2 layers.

The diffusion coefficient and electroactive surface area of the as-synthesized Ti-TiO_2-rGO composite structures and Ti-TiO_2 layers, respectively, were calculated based on the Randles–Sevcik Equation (1) [42]:

$$I_p = 2.69 \times 10^5 A D^{1/2} n^{3/2} v^{1/2} C \quad (1)$$

where: *A*–represents the geometric surface area of the sensor (cm^2); *n*–represents the number of participating electrons in the reaction, equal to 1; *D*–represents the diffusion coefficient of the molecules in solution; *C*–is the molar concentration of $K_3Fe(CN)_6$ in the solution (i.e., 4 mM); *v*–represents the scanning speed ($V\ s^{-1}$). The obtained results are presented in Table 2.

Electrochemical measurements show that, for all the Ti-TiO_2-rGO composite structures, an electroactive surface area greater than the geometric one was obtained, a fact that recommends these structures for further electrochemical detection applications (Figure 6). As presented in Table 2, the largest electroactive surface area was obtained for Ti-TiO_2-rGO-1h, and, for Ti-TiO_2-rGO-2h and Ti-TiO_2-rGO-3h, the electroactive area is almost similar, compared with Ti-TiO_2 layers where the electroactive area is smaller than the geometrical area. The electrochemical characterization of the supporting electrolyte, as well as in the presence of potassium ferro/ferricyanide, confirmed the resistance of the composite film on the structure surface during the electrochemical tests.

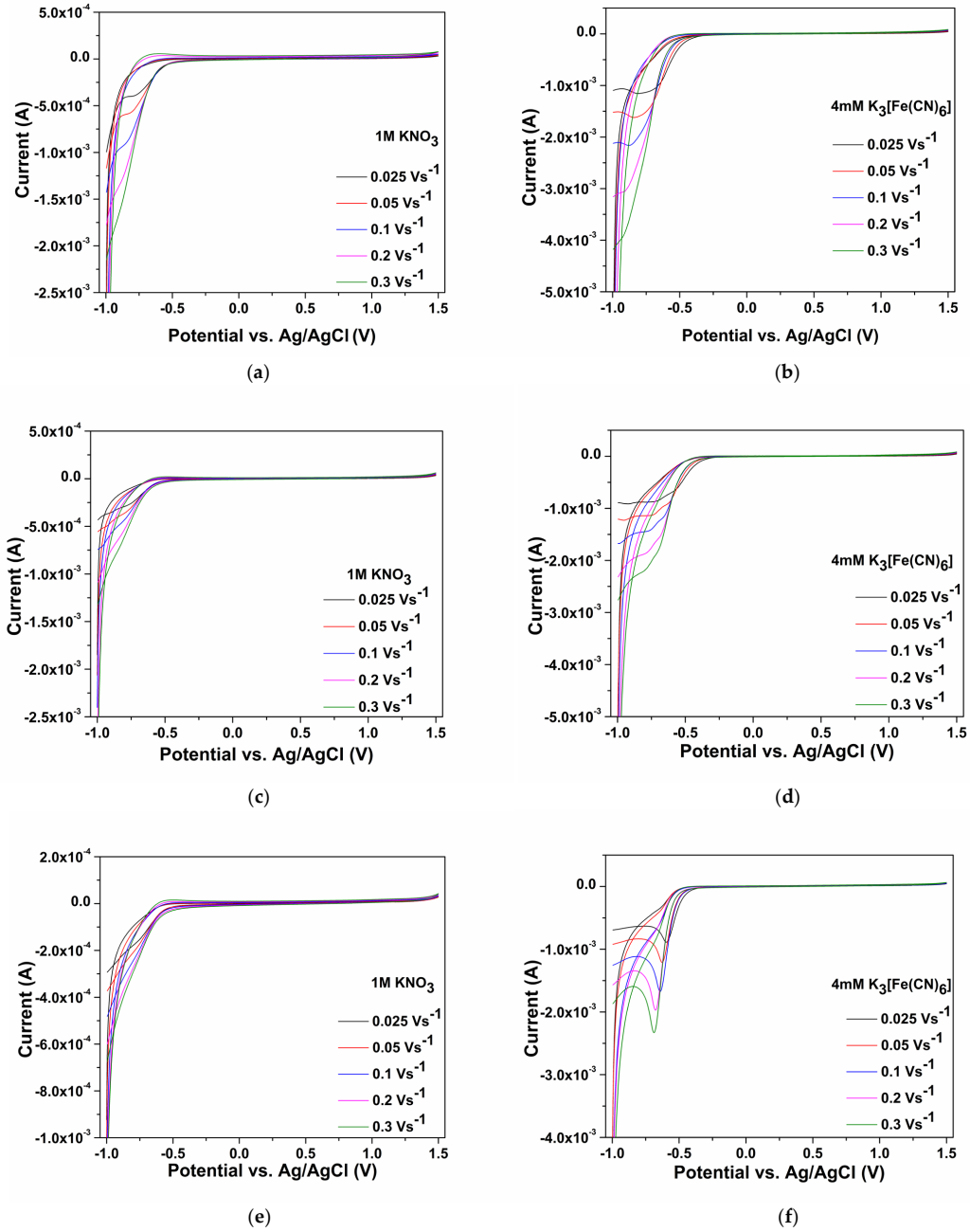

Figure 6. Cyclic voltammograms for the (**a**) Ti-TiO_2-rGO-1h, (**c**) Ti-TiO_2-rGO-2h, and (**e**) Ti-TiO_2-rGO-3h composite structures, recorded in a 1M KNO_3 electrolyte support and (**b**) Ti-TiO_2-rGO-1h, (**d**) Ti-TiO_2-rGO-2h, (**f**) Ti-TiO_2-rGO-3h composite structures in the presence of 4mM $K_3Fe(CN)_6$.

Table 2. The apparent diffusion coefficient and electroactive surface area of the tested Ti-TiO_2 layers and the Ti-TiO_2-rGO composite structures.

Composite Structure	Geometrical Surface Area (cm^2)	Electroactive Surface Area (cm^2)	Diffusion Coefficient ($cm^2\ s^{-1}$)
Ti-TiO_2-1h	1.8	0.58	7.09×10^{-7}
Ti-TiO_2-rGO-1h	0.99	1.31	3.55×10^{-6}
Ti-TiO_2-2h	1.8	0.57	6.78×10^{-7}
Ti-TiO_2-rGO-2h	0.70	0.87	1.60×10^{-6}
Ti-TiO_2-3h	1.8	0.74	1.13×10^{-7}
Ti-TiO_2-rGO-3h	0.30	0.93	1.80×10^{-6}

Moreover, electrochemical impedance spectroscopy (EIS) experiments were performed for the Ti-TiO_2-rGO-1h composite structure that exhibited the highest electroactive surface area. The supporting electrolyte used for the EIS tests was 0.1 M Na_2SO_4, which was appropriate for the further electrochemical detection applications of the obtained electrodes. The impedance diagrams recorded in a 0.1 M Na_2SO_4 supporting electrolyte and a frequency range between 100 kHz and 0.1 Hz for the Ti-TiO_2-1h and Ti-TiO_2-rGO-1h structures were fit, considering the electrical equivalent circuits shown in Figure 7.

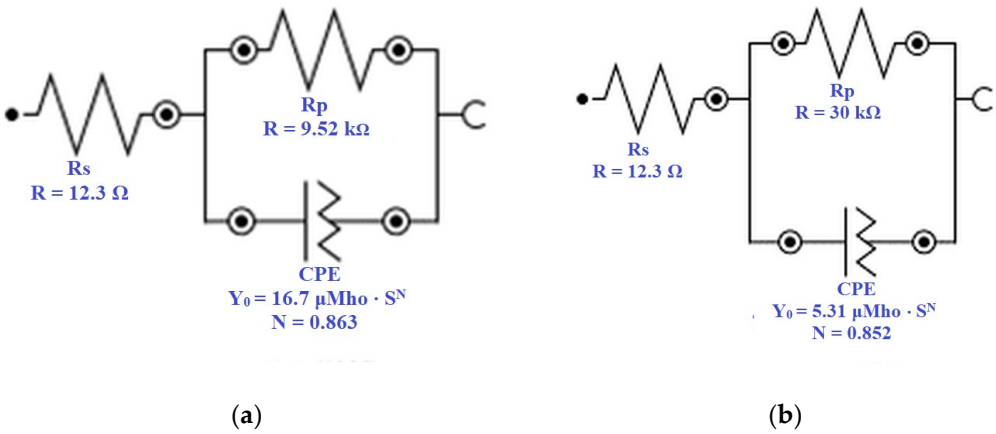

(**a**) (**b**)

Figure 7. Electrical equivalent circuits for the **(a)** Ti-TiO_2-1h and **(b)** Ti-TiO_2-rGO-1h structures.

Both circuits include the following electronic elements: R_s is the electrolyte resistance between the working and reference electrodes, and R_p is the charge transfer resistance and a CPE (constant phase element) that simulates the nonideal behavior of the capacitor. The charge transfer resistance for Ti-TiO_2-rGO-1h increased compared with Ti-TiO_2-1h, while the capacitance value decreased in the Ti-TiO_2-rGO-1h equivalent circuit, confirming the role of the rGO on the electrode surface.

4. Conclusions

In summary, the innovative in situ deposition of rGO was approached by synthesizing Ti-TiO_2-rGO composite structures on Ti foil through a one-step microwave-assisted hydrothermal process. The use of TTIP as a dispersion matrix facilitates the deposition of the films onto the layers. The microwave-assisted hydrothermal method for obtaining the composite structures proved to be a feasible and easy-to-use method for the development of Ti-TiO_2-rGO composite structures. The morphological characteristics determined by SEM analysis showed the clear and defined oriented growth of the Ti-TiO_2 layers, and the rGO films were successfully deposited onto the Ti-TiO_2 layers. From the *I-V* measurements on the established TiO_2-rGO junction, it was shown that an increase in etching time could move the junction from an ideal position. In this study, a strong correlation was established between the ideality factor of the Ti-TiO_2-rGO-1h composite structure and the increase in the electroactive surface area. Moreover, the EIS measurements confirmed the important role of the rGO deposited onto the electrode surface, showing a higher charge transfer resistance for Ti-TiO_2-rGO-1h compared to Ti-TiO_2-1h. The results obtained in this study offer new perspectives on achieving high-performance and cost-effective Ti-TiO_2-rGO structures that are usable in the development of both electrochemical electrodes and gas sensors.

Supplementary Materials: The following supporting information can be downloaded at: https://www.mdpi.com/article/10.3390/coatings12121805/s1, Figure S1: Cyclic voltammograms recorded in 1M KNO_3 electrolyte support and in the presence of 1M $KMnO_3(CN)_6$ for Ti-TiO_2-1h **(a)**; Ti-TiO_2-2h **(c)**; Ti-TiO_2-3h **(e)** layersand in 4mM $K_3Fe(CN)_6$ for Ti-TiO_2-1h **(b)**; Ti-TiO_2-2h **(d)**; Ti-TiO_2-3h **(f)** layers.

Author Contributions: Conceptualization, C.B.; Methodology, C.L., M.N., C.O., A.P. and C.B.; Validation, C.B.; Investigation, C.L., M.N., C.O., A.P. and C.B.; Writing—original draft, C.L., M.N., C.O., A.P., S.C. and C.B.; Supervision, C.B. All authors have read and agreed to the published version of the manuscript.

Funding: This work was supported by a grant of the Ministry of Research, Innovation and Digitization, CNCS-UEFISCDI, project number PN-III-P1-1.1-TE-2021-0963, within PNCDI III, with contract number TE13/2022 (DD-CyT); by Project "Network of excellence in applied research and innovation for doctoral and postdoctoral programs/InoHubDoc", project co-funded by the European Social Fund financing agreement no. POCU/993/6/13/153437, and partially by project code PN 19 22 04 01 TINSME, 40 N/2019.

Institutional Review Board Statement: Not applicable.

Informed Consent Statement: Not applicable.

Data Availability Statement: Not applicable.

Conflicts of Interest: The authors declare no conflict of interest. The funders had no role in the design of the study; in the collection, analyses, or interpretation of data; in the writing of the manuscript, or in the decision to publish the results.

References

1. Schedin, F.; Geim, A.K.; Morozov, S.V.; Hill, E.W.; Blake, P.; Katsnelson, M.I.; Novoselov, K.S. Detection of individual gas molecules adsorbed on graphene. *Nat. Mater.* **2007**, *6*, 652–655. [CrossRef] [PubMed]
2. Huang, X.; Qi, X.; Boey, F.; Zhang, H. Graphene-based composites. *Chem. Soc. Rev.* **2012**, *41*, 666–686. [CrossRef] [PubMed]
3. Wei, Y.; Gao, C.; Meng, F.-L.; Li, H.-H.; Wang, L.; Liu, J.-H.; Huang, X.-J. SnO_2/reduced graphene oxide nanocomposite for the simultaneous electrochemical detection of Cadmium(II), Lead(II), Copper(II), and Mercury(II): An interesting favorable mutual interference. *J. Phys.Chem. C* **2011**, *116*, 1034–1041. [CrossRef]
4. Khun Khun, K.; Mahajan, A.; Bedi, R.K. Nanostructured Sb doped SnO_2 thick films for room temperature NH_3 sensing. *Chem. Phys. Lett.* **2010**, *492*, 119–122. [CrossRef]
5. Sennik, E.; Kilinc, N.; Ozturk, Z.Z. Electrical and VOC sensing properties of anatase and rutile TiO_2 nanotubes. *J. Alloys Compd.* **2014**, *616*, 89–96. [CrossRef]
6. Sun, Z.; Huang, D.; Yang, Z.; Li, X.; Hu, N.; Yang, C.; Wei, H.; Yin, G.; He, D.; Zhang, Y. ZnO Nanowire-Reduced Graphene Oxide Hybrid Based Portable NH_3 Gas Sensing Electron Device. *IEEE Electron Device Lett.* **2015**, *36*, 1376–1379. [CrossRef]
7. Mohammadi-Manesh, E.; Vaezzadeh, M.; Saeidi, M. Cu- and CuO-decorated graphene as a nanosensor for H_2S detection at room temperature. *Surf. Sci.* **2015**, *636*, 36–41. [CrossRef]
8. Urasinska-Wojcik, B.; Vincent, T.A.; Chowdhury, M.F.; Gardner, J.W. Ultrasensitive WO_3 gas sensors for NO_2 detection in air and low oxygen environment. *Sens. Actuators B Chem.* **2017**, *239*, 1051–1059. [CrossRef]
9. Geng, X.; You, J.; Wang, J.; Zhang, C. Visible light assisted nitrogen dioxide sensing using tungsten oxide - Graphene oxide nanocomposite sensors. *Mater. Chem. Phys.* **2017**, *191*, 114–120. [CrossRef]
10. Patil, S.P.; Patil, V.L.; Shendage, S.S.; Harale, N.S.; Vanalakar, S.A.; Kim, J.H.; Patil, P.S. Spray pyrolyzed indium oxide thick films as NO_2 gas sensor. *Ceram. Int.* **2016**, *42*, 16160–16168. [CrossRef]
11. Xu, T.; Pei, Y.; Liu, Y.; Wu, D.; Shi, Z.; Xu, J.; Tian, Y.; Li, X. High-response NO2 resistive gas sensor based on bilayer MoS2 grown by a new two-step chemical vapor deposition method. *J. Alloys Compd.* **2017**, *725*, 253–259. [CrossRef]
12. Ghule, B.G.; Shinde, N.M.; Raut, S.D.; Gore, S.K.; Shaikh, S.F.; Ekar, S.U.; Ubaidullah, M.; Pak, J.J.; Mane, R.S. Self-assembled α-Fe_2O_3-GO nanocomposites: Studies on physical, magnetic and ammonia sensing properties. *Mater. Chem. Phys.* **2022**, *278*, 125617. [CrossRef]
13. Zhang, X.; Zhong, H.; Xu, L.; Wang, S.; Chi, H.; Pan, Q.; Zhang, G. Fabrication of Co_3O_4/PEI-GO composites for gas-sensing applications at room temperature. *Mater. Res. Bull.* **2018**, *102*, 108–115. [CrossRef]
14. Jamjoum, H.A.A.; Umar, K.; Adnan, R.; Razali, M.R.; Mohamad Ibrahim, M.N. Synthesis, Characterization, and Photocatalytic Activities of Graphene Oxide/metal Oxides Nanocomposites: A Review. *Front. Chem.* **2021**, *9*, 752276. [CrossRef] [PubMed]
15. Sahoo, S.K.; Hota, G. Functionalization of graphene oxide with metal oxide nanomaterials: Synthesis and applications for the removal of inorganic, toxic, environmental pollutants from water. *Micro Nano Technol.* **2020**, 299–326. [CrossRef]
16. Yoon, Y.; Park, W.K.; Hwang, T.M.; Yoon, D.H.; Yang, W.S.; Kang, J.W. Comparative evaluation of magnetite-graphene oxide and magnetite-reduced graphene oxide composite for As(III) and As(V) removal. *J. Hazard. Mater.* **2016**, *304*, 196–204. [CrossRef]
17. Chandra, V.; Park, J.; Chun, Y.; Woo Lee, J.; Hwang, I.-C.; Kim, K.S. Water-Dispersible Magnetite-Reduced Graphene Oxide Composites for Arsenic Removal. *ACS Nano* **2010**, *4*, 3979–3986. [CrossRef]
18. Fan, L.; Luo, C.; Sun, M.; Li, X.; Qiu, H. Highly selective adsorption of lead ions by water-dispersible magnetic chitosan/graphene oxide composites. *Colloids Surf. B Biointerfaces* **2013**, *103*, 523–529. [CrossRef]

19. Liu, M.; Wen, T.; Wu, X.; Chen, C.; Hu, J.; Li, J.; Wang, X. Synthesis of porous Fe_3O_4 hollow microspheres/graphene oxide composite for Cr(VI) removal. *Dalton Trans.* **2013**, *42*, 14710–14717. [CrossRef]
20. Liu, J.; Ge, X.; Ye, X.; Wang, G.; Zhang, H.; Zhou, H.; Zhang, Y.; Zhao, H. 3D graphene/δ-MnO2 aerogels for highly efficient and reversible removal of heavy metal ions. *J. Mater. Chem. A* **2016**, *4*, 1970–1979. [CrossRef]
21. Babu, C.M.; Vinodh, R.; Sundaravel, B.; Abidov, A.; Peng, M.M.; Cha, W.S.; Jang, H.-T. Characterization of reduced graphene oxide supported mesoporous Fe_2O_3/TiO_2 nanoparticles and adsorption of As(III) and As(V) from potable water. *J. Taiwan Inst. Chem. Eng.* **2016**, *62*, 199–208. [CrossRef]
22. Mohan, S.; Kumar, V.; Singh, D.K.; Hasan, S.H. Synthesis and characterization of rGO/ZrO_2 nanocomposite for enhanced removal of fluoride from water: Kinetics, isotherm, and thermodynamic modeling and its adsorption mechanism. *RSC Adv.* **2016**, *6*, 87523–87538. [CrossRef]
23. Wu, S.; Yin, Z.; He, Q.; Huang, X.; Zhou, X.; Zhang, H. Electrochemical deposition of semiconductor oxides on reduced rraphene oxide-based flexible, transparent, and conductive electrodes. *J. Phys. Chem. C* **2010**, *114*, 11816–11821. [CrossRef]
24. Tai, H.; Yuan, Z.; Zheng, W.; Ye, Z.; Liu, C.; Du, X. ZnO nanoparticles/reduced graphene oxide bilayer thin films for improved NH_3-sensing performances at room temperature. *Nanoscale Res. Lett.* **2016**, *11*, 130. [CrossRef]
25. Fauzi, A.S.A.; Hamidah, N.L.; Kitamura, S.; Kodama, T.; Sonda, K.; Putri, G.K.; Shinkai, T.; Ahmad, M.S.; Inomata, Y.; Quitain, A.T.; et al. Electrochemical detection of ethanol in air using graphene oxide nanosheets combined with Au-WO_3. *Sensors* **2022**, *22*, 3194. [CrossRef]
26. Zhang, D.; Jiang, C.; Liu, J.; Cao, Y. Carbon monoxide gas sensing at room temperature using copper oxide-decorated graphene hybrid nanocomposite prepared by layer-by-layer self-assembly. *Sens. Actuators B Chem.* **2017**, *247*, 875–882. [CrossRef]
27. Zhang, Q.; Zhang, Y.; Meng, Z.; Tong, W.; Yu, X.; An, Q. Constructing the magnetic bifunctional graphene/titania nanosheet-based composite photocatalysts for enhanced visible-light photodegradation of MB and electrochemical ORR from polluted water. *Sci. Rep.* **2017**, *7*, 12296. [CrossRef]
28. Wang, P.; Ao, Y.; Wang, C.; Hou, J.; Qian, J. Enhanced photoelectrocatalytic activity for dye degradation by graphene-titania composite film electrodes. *J. Hazard. Mater.* **2012**, *223–224*, 79–83. [CrossRef]
29. Arfin, T.; Rangari, S.N. Graphene oxide–ZnO nanocomposite modified electrode for the detection of phenol. *Anal. Methods* **2018**, *10*, 347–358. [CrossRef]
30. Muniandy, S.; Teh, S.J.; Appaturi, J.N.; Thong, K.L.; Lai, C.W.; Ibrahim, F.; Leo, B.F. A reduced graphene oxide-titanium dioxide nanocomposite based electrochemical aptasensor for rapid and sensitive detection of Salmonella enterica. *Bioelectrochemistry* **2019**, *127*, 136–144. [CrossRef]
31. Vajedi, F.; Dehghani, H. The characterization of TiO_2-reduced graphene oxide nanocomposites and their performance in electrochemical determination for removing heavy metals ions of cadmium(II), lead(II) and copper(II). *Mater. Sci. Eng. B* **2019**, *243*, 189–198. [CrossRef]
32. Nicolaescu, M.; Bandas, C.; Orha, C.; Şerban, V.; Lazău, C.; Căprărescu, S. Fabrication of a UV photodetector based on n-TiO_2/p-$CuMnO_2$ heterostructures. *Coatings* **2021**, *11*, 1380. [CrossRef]
33. Xiang, C.; Li, M.; Zhi, M.; Manivannan, A.; Wu, N. Reduced graphene oxide/titanium dioxide composites for supercapacitor electrodes: Shape and coupling effects. *J. Mater. Chem.* **2012**, *22*, 19161. [CrossRef]
34. Wang, H.; Guan, C.; Wang, X.; Fan, H.J. A high energy and power Li-ion capacitor based on a TiO_2 nanobelt array anode and a graphene hydrogel cathode. *Small* **2015**, *11*, 1470–1477. [CrossRef]
35. Zhao, C.; Ju, P.; Wang, S.; Zhang, Y.; Min, S.; Qian, X. One-step hydrothermal preparation of TiO_2/RGO/$Ni(OH)_2$/NF electrode with high performance for supercapacitors. *Electrochim. Acta* **2016**, *218*, 216–227. [CrossRef]
36. Romeiro, F.C.; Silva, S.C.; Nossol, E.; Lima, R.C. One step microwave-hydrothermal synthesis of rGO–TiO_2 nanocomposites for enhanced electrochemical oxygen evolution reaction. *New J. Chem.* **2020**, *44*, 6825–6832. [CrossRef]
37. Deb, P.; Dhar, J.C. Boosted photoresponsivity using silver nanoparticle decorated TiO_2 nanowire/reduced graphene oxide thin-film heterostructure. *Nanotechnology* **2020**, *31*, 285202. [CrossRef]
38. CİMİLİİ ÇAtir, F.E. Properties of a facile growth of spray pyrolysis-based rGO films and device performance for Au/rGO/n-InP Schottky diodes. *J. Mater. Sci. Mater. Electron.* **2020**, *32*, 611–622. [CrossRef]
39. Sah, C.-T.; Noyce, R.N.; Shockley, W. Carrier generation and recombination in P-N junctions and P-N junction characteristics. *Proc. IRE* **1957**, *45*, 1228–1243. [CrossRef]
40. Trenczek-Zajac, A. Influence of etching on structural, optical and photoelectrochemical properties of titanium oxides obtained via thermal oxidation. *Mater. Sci. Semicond. Process.* **2018**, *83*, 159–170. [CrossRef]
41. Brötzmann, M.; Vetter, U.; Hofsäss, H. BN/ZnO heterojunction diodes with apparently giant ideality factors. *J. Appl. Phys.* **2009**, *106*. [CrossRef]
42. González-Meza, O.A.; Larios-Durán, E.R.; Gutiérrez-Becerra, A.; Casillas, N.; Escalante, J.I.; Bárcena-Soto, M. Development of a Randles-Ševčík-like equation to predict the peak current of cyclic voltammetry for solid metal hexacyanoferrates. *J. Solid State Electrochem.* **2019**, *23*, 3123–3133. [CrossRef]